

Seismic response of high concrete face rockfill dams subjected to non-uniform input motion

Yu Yao¹ · Rui Wang^{2,3}  · Tianyun Liu^{2,4} · Jian-Min Zhang^{2,3}

Received: 21 November 2016 / Accepted: 22 January 2018 / Published online: 6 March 2018
© Springer-Verlag GmbH Germany, part of Springer Nature 2018

Abstract

Analysis of the seismic response of high CFRDs under non-uniform ground motion input is conducted using a novel non-uniform input motion calculation method combined with nonlinear FEM. The non-uniform input motion calculation method and its basic assumption are validated. The response of CFRDs under uniform and non-uniform input is compared to discuss the necessity of conducting seismic analysis of high CFRDs under realistic non-uniform ground motion input. When the acceleration at the surface of the free field for dynamic simulations with uniform and non-uniform input is kept consistent, the seismic response of CFRDs under non-uniform input is in general significantly smaller, while the dynamic tensile stress around the edges of the concrete face slab is greater. The simulation results suggest that non-uniformity of the ground motion input has important effects on the seismic response of high CFRDs and should be considered in the seismic design of CFRDs. The influence of the incident angle of seismic waves is also investigated, with results indicating that the influence is waveform dependent, while being frequency independent.

Keywords Angle of incidence · High CFRD · Non-uniform input · Seismic response · Wave theory

1 Introduction

Seismic safety is of great importance to the design and construction of concrete face rockfill dams (CFRD) due to the possible catastrophic consequences associated with dam failures [8, 30, 36]. Currently, most design codes and guidelines assume the input ground motion to be uniform in the seismic evaluation of CFRDs (e.g., [19]). However, due to the effects of traveling wave and 3D site characteristics, the actual ground motion at the base of the dam could be significantly non-uniform. For instance, the

acceleration time histories recorded during the 2011 Tohoku earthquake at the Tatsumi and Hachieda stations only 800 m apart [24] are drastically different, with differences of 61, – 22 and 123% in the peak acceleration in the east–west, north–south and vertical directions, respectively. These records suggest that the ground motion can be significantly non-uniform within a range of several hundred meters, which is in the same order of magnitude as the axis length and width of high CFRDs. For example, the Shuibuya CFRD in China has a maximum height of 233 m, length of 675 m and width of 667 m [53]. Possible non-uniformity of the input ground motion at the base of such large dams during earthquakes could cause the actual seismic dam response to differ significantly from the response obtained based on uniform ground motion input adopted by current design methods [19]. Although there are only few records of high CFRDs' performance during major earthquakes, the damage of the Zipingpu CFRD during the 2008 Wenchuan earthquake has rung an alarm bell for the seismic design of high CFRDs in earthquake-prone areas. Zhang et al. [48] investigated the damage of the 156-m-high Zipingpu CFRD after the Wenchuan earthquake and found that although the overall damage of

✉ Rui Wang
wangrui_05@mail.tsinghua.edu.cn

¹ China Renewable Energy Engineering Institute, Beijing 100084, China

² Department of Hydraulic Engineering, Tsinghua University, Beijing 100084, China

³ National Engineering Laboratory for Green and Safe Construction Technology in Urban Rail Transit, Tsinghua University, Beijing 100084, China

⁴ State Key Laboratory of Hydroscience and Engineering, Tsinghua University, Beijing 100084, China

the dam was minor and repairable, the propagation of seismic wave may have led to the dislocation and non-uniform deformation of the dam near the abutments, which poses a major threat to the seepage control system. As numerous high CFRDs are being planned in some of the most seismically active areas in China [38], there is an urgent need to study the seismic response of CFRDs subjected to non-uniform ground motion input.

Currently, some statistic methods have been adopted to obtain the non-uniform ground motion input in a few design codes for large structures (e.g., [14]). A coherency model for the wave propagation based on existing earthquake records is used (e.g., [10, 32, 35]). For better description of spatial variability, some researchers have further developed models for the propagation of seismic waves from the source to the ground surface (e.g., [2, 46]). However, such models are unable to take into account the effect of the scattering of the ground surface, which could be influential when the ground surface is significantly irregular, limiting the application of such methods on high CFRDs with significantly irregular valley surface.

To consider the seismic response of dams under non-uniform input, two major categories of numerical analysis methods, which take the shape of the valley surface into account, have been developed (e.g., [16, 28, 29, 31, 49, 50]). The first group of methods obtains the displacement field at the base of the dam by solving the scattering problem of the surface irregularity, which is then input at the base of the dam to conduct seismic analysis. The key component of such methods lies within the way that the scattering problem in the half-space is solved. For arbitrary shape valleys, the boundary element method has often been used to solve the scattering problem (e.g., [49, 50]), but it tends to encounter problems with singularity [17] and computation efficiency in obtaining the fundamental solution in the half-space [1]. Scaled boundary finite element method has also been applied to solve the scattering problem in the half-space (e.g., [16, 31]), though it often has difficulties in determining the scaling center [21]. The wave function expansion method [28, 29] and the fictitious source method [22, 40] have also been used, but both have limitations in accuracy and efficiency [44].

The other category of methods incorporates an appropriate amount of the bedrock in the seismic dam analysis model with special considerations for the truncated boundaries. To achieve this, simple elastic or viscoelastic shear beam models [6, 7, 18, 26] and high fidelity finite element models with artificial boundary conditions have been developed [3, 41, 47, 52]. Methods in this category are generally more computationally costly and often experience difficulties in fully eliminating the reflection of the outgoing wave at the boundaries of the model, especially when the model is considered to be nonlinear.

Applying the above methods, the seismic response of dams under non-uniform and uniform input motion has been compared by several researchers. Some studies have suggested that the seismic response of the dam under non-uniform input motion is smaller than that under uniform input [3, 6, 7, 18, 26, 52], while some others found the response to be larger under non-uniform input motion [10]. There have also been studies reporting that the influence of non-uniform input could be different for different aspects of seismic response (e.g., acceleration, stress, strain, settlement and lateral displacement), with some aspects of seismic response being larger under non-uniform input, and others being larger under uniform input [31, 32, 35].

As a natural outcome of taking the more realistic non-uniform input into consideration, the role of the incident wave direction in the response of the dam has also been investigated. Dakoulas indicated that under incident SH waves, the peak acceleration reaches a maximum at an incident angle (i.e., the angle between the incident wave direction and the vertical direction) of about 30° for a rectangle canyon, while it increases monotonically with the increase in the incident angle for a semicircle canyon [6, 7]. Wu suggested that the permanent deformation of dams increases with the increase in the incident angle under P waves; while under SV waves, the deformation reaches its peak when the incident angle is between 30° and 45° [41]. In contrast, Zhang suggested that dam deformation decreases monotonically with the increase in the incident angle under SV waves [47].

Although existing studies have provided valuable insights into the response of dams under non-uniform input motion, current non-uniform input motion analysis methods for CFRDs still require further development, and the conclusions drawn from current studies exhibit clear discrepancies. These problems indicate that further research should be conducted to develop computationally efficient high fidelity analysis methods that reflect the non-uniform nature of the input motion, and to analyze the seismic response of CFRDs under non-uniform input motion.

The current work focuses on the seismic response of high CFRDs under non-uniform seismic motion, which is studied by applying the non-uniform motion obtained using a newly developed semi-analytical solution at the base of high CFRDs in 3D nonlinear FEM analysis. Yao et al. [44] proposed a new method for calculating the scattering of waves in an infinite half-space with a random shaped valley, which has advantages in computational efficiency and numerical stability. The method can be used to solve the displacement time histories of any position on the base of a CFRD and hence provide the non-uniform ground motion input. The solution method developed by Yao et al. [44] is here extended to 3D and validated in Sect. 2 of this paper, after which the FEM dynamic CFRD analysis method is

provided. Section 3 compares the seismic response of CFRDs under the non-uniform and uniform input based on the result of the dynamic analysis. Section 4 provides an analysis of the influence of the incident angle on the seismic response of CFRDs based on FEM simulation results and the wave theory.

2 Methodology

2.1 Basic assumption

As a means to conduct nonlinear seismic analysis on high CFRDs subjected to non-uniform excitation, an appropriate method for obtaining the input at the base of the dam is here developed, with the bedrock considered linear elastic. As the modulus of the rockfill is around two orders of magnitudes smaller than that of the bedrock [31], it is reasonable to make the basic assumption that the CFRD's influence on the seismic displacement field at the surface of the bedrock is very limited, and the difference in displacement between that at the base of the CFRD and that of the valley without the dam should be negligible [25]. Based on this assumption, a displacement field solved from the elastic wave scattering by an empty valley (surface irregularities) in a half-space can be used as the input displacement for the non-uniform input seismic analysis of the CFRD at the same site. Using this proposed approach, seismic analysis of high CFRDs subjected to non-uniform excitation can be decomposed into a two-step problem (Fig. 1). Step 1 is to develop a solution for the scattering of seismic waves by an irregular surface (i.e., the empty valley), providing the non-uniform displacement input at the base of the CFRD. Step 2 is to input the non-uniform motion and conduct dynamic analysis of the CFRD.

In order to validate this basic assumption, two hypothetical 3D linear elastic FEM models of the bedrock of the valley with and without a CFRD on top are constructed as shown in Fig. 2. The material parameters used for the bedrock and CFRD rockfill and concrete face slab are chosen to be close to typical values of each respective material and are listed in Table 1. The nonlinearity of the materials is not considered in this validation example. A pulse along with the valley direction (y) acceleration time history following that of Fig. 3 is input into each model at the bottom boundary of the model. The side boundaries parallel to the valley are fixed against displacement in the normal direction (x), while tied boundary condition is implemented on the two sides perpendicular to the valley. The choice of model size and input motion guarantees that the reflection of the incident wave caused by the truncated boundaries cannot arrive at the base of the dam during the entire simulation process, and hence does not affect the

motion at the base of the dam. Figure 4 shows the peak y direction acceleration distribution along the intersection of the base and axis planes of the dam for both the models with and without the CFRD, which suggests that the influence of the dam on the peak acceleration at its base is very small. Furthermore, the acceleration time histories in points A and B are plotted in Fig. 5, at the base and crest, respectively, which also show very little difference for the models with and without the CFRD. This analysis validates that basic assumption made in this study.

2.2 Non-uniform input motion calculation method

A new 2D semi-analytical method developed by Yao et al. [44] can be extended into 3D to provide a solution for the scattering of seismic waves by the irregular river valley, considering the bedrock as a uniform elastic medium. The solution of the problem should satisfy the wave equations within the bedrock domain, zero traction at the surface of the domain and the radiation boundary conditions at infinity (Fig. 1b). In order to satisfy these conditions, the three main steps of the solution method are concisely described in the following paragraphs. More details of the method formulation in 2D can be found in the work of Yao et al. [44].

1. Obtain a general series solution which satisfies the wave equation within the domain and the free-surface boundary condition of a half-space. Wave functions are able to satisfy the wave equation within the domain but does not comply with the free-surface boundary condition. In order to satisfy both, a virtual force opposite to that caused by the wave function at the free surface is applied. By combining the displacement field generated by a series of wave functions and their respective virtual forces, a general series solution that complies with both the wave equation within the domain and the free-surface boundary condition is obtained. Note that the coefficients of this series solution are here still undetermined, and the displacement and stress at infinity are zero.
2. Obtain the solution for the incidence of a random wave in half-space. This solution is readily available analytically for waves of any frequency and incident angle [44] and satisfies with the free-surface boundary condition and the boundary condition at infinity.
3. Determine the coefficients of the general series solution obtained in step 1, so that the combination of the solutions obtained in steps 1 and 2 satisfies the zero traction boundary condition at the irregular surface. The free-surface boundary condition is already satisfied by both the solutions in steps 1 and 2. The boundary condition at infinity is satisfied by the solution in step 2, while the solution for infinity in

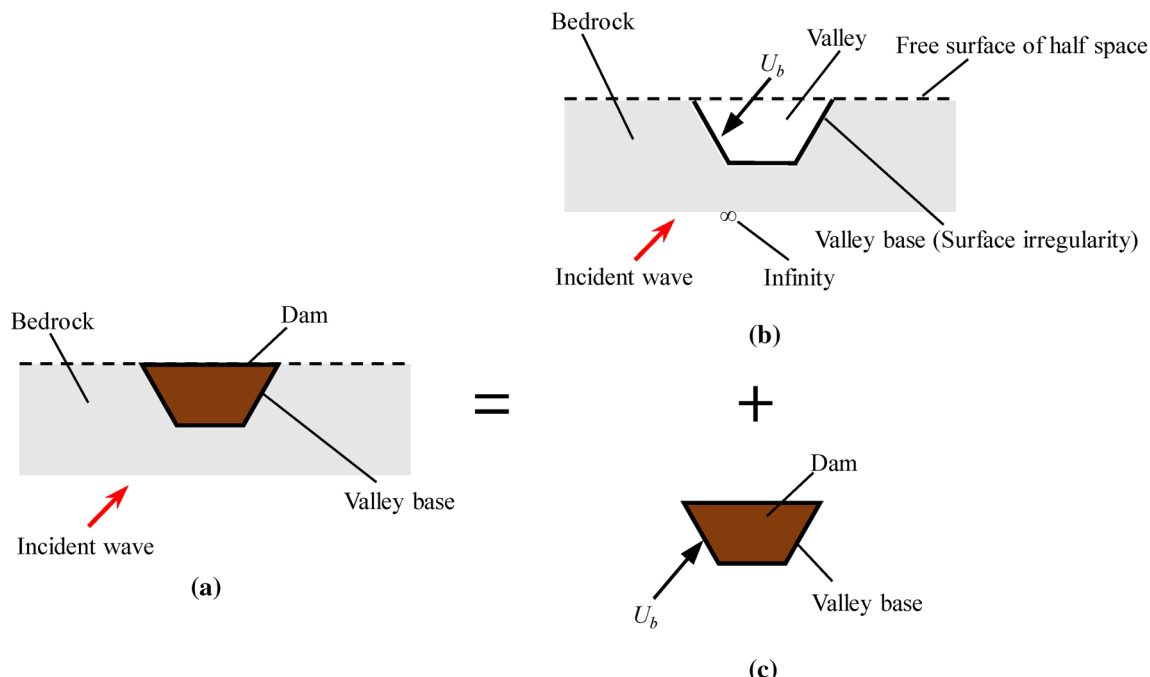


Fig. 1 The decomposition of **a** the seismic analysis of high CFRDs subjected to non-uniform excitation into: **b** Step 1, solution for the scattering of seismic waves by an irregular surface. **c** Step 2, dynamic analysis of the CFRD with non-uniform input from step 1. ‘ U_b ’ stands for the displacement field obtained from the solution of the scattering problem of the empty valley as the input displacement at the base of the dam

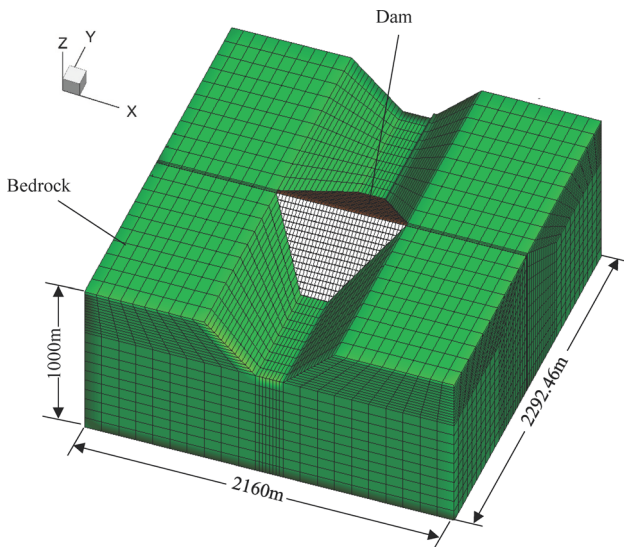


Fig. 2 FEM model of hypothetical dam–bedrock system. For simulation of the bedrock alone, the dam is removed from the model

Table 1 Parameters for method validation

Materials	Young's modulus (GPa)	Poisson's ratio	Density (kg/m ³)
Bedrock	15	0.25	2650
Face slab	30	0.167	2400
Rockfill	0.15	0.25	2214

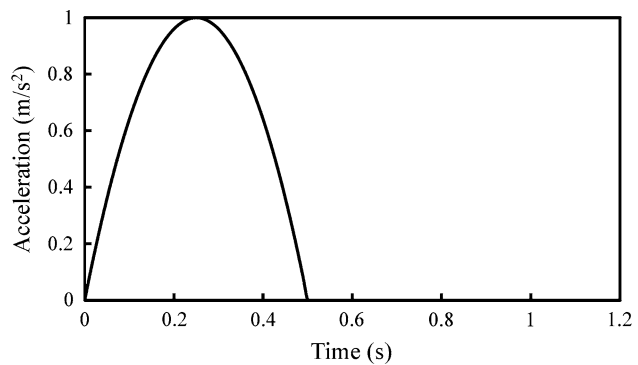


Fig. 3 Input acceleration time history for method validation

step 1 is zero. Hence, the combined solution obtained in step 3 complies with all of the boundary conditions and the wave equations within the domain.

In step 1, spherical wave functions should be used for a 3D problem [25]:

$$\left. \begin{aligned} \phi_{\text{sph}} &= \sum_{n=0}^N \sum_{m=0}^n A_n^m Z_n^i(pr) P_n^m(\cos \theta) \exp[i(m\varphi - \omega t)] \\ \psi_{\text{sph}} &= \sum_{n=0}^N \sum_{m=0}^n B_n^m Z_n^i(sr) P_n^m(\cos \theta) \exp[i(m\varphi - \omega t)] \\ \chi_{\text{sph}} &= \sum_{n=0}^N \sum_{m=0}^n C_n^m Z_n^i(sr) P_n^m(\cos \theta) \exp[i(m\varphi - \omega t)] \end{aligned} \right\} \quad (1)$$

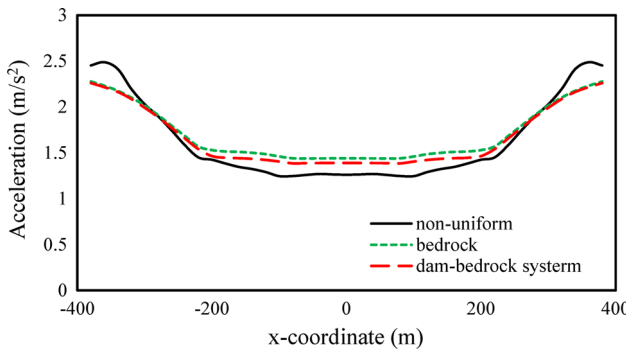


Fig. 4 Comparison of the peak y acceleration distribution along the intersection of the base and axis plane of the dam

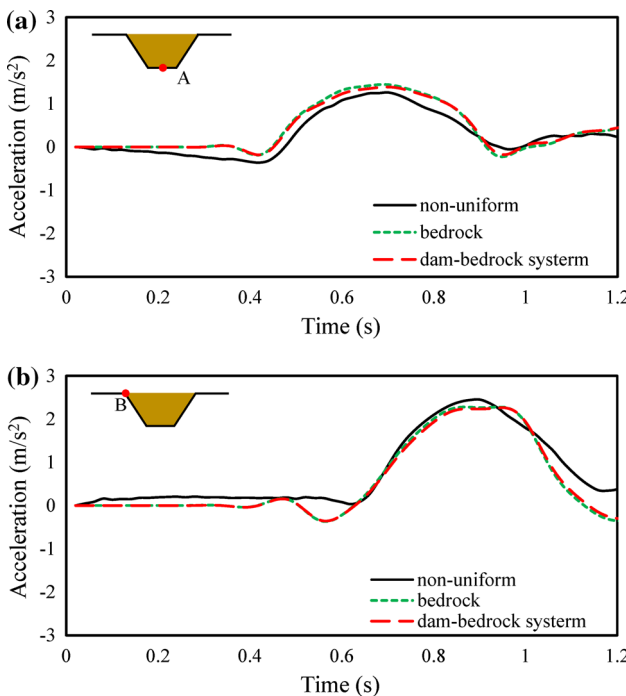


Fig. 5 The contrast of the acceleration time history for the typical points A and B: **a** acceleration time history for the typical point A, **b** acceleration time history for the typical point B

where Z stands for the spherical Bessel function of the second kind; P stands for the associated Legendre function; p stands for the wave number of P wave; s stands for the wave number of shear wave; t stands for time; r , θ and ϕ are the coordinates in the spherical coordinate system; m and n are integers; and A_n^m , B_n^m and C_n^m are coefficients.

Solving for the displacement field in a 3D half-space under the applied virtual load in step 1 is a 3D Lamb's problem [20], which can be solved using the Hankel transformation [45], with the potential functions in the cylindrical coordinate system being [25]:

$$\left. \begin{aligned} \psi_{\text{cyl}} &= \varphi = A(k)J_n(kr)e^{int\theta}e^{i\gamma_p z} \\ \psi_{\text{cyl}}^1 &= \psi = B(k)J_n(kr)e^{int\theta}e^{i\gamma_p z} \\ \psi_{\text{cyl}}^2 &= \chi = C(k)J_n(kr)e^{int\theta}e^{i\gamma_p z} \end{aligned} \right\} \quad (2)$$

where $\gamma_p^2 = p^2 - k^2$, $\gamma_s^2 = s^2 - k^2$ and k stand for the wave number ranking from 0 to $+\infty$. The coefficients $A(k)$, $B(k)$ and $C(k)$ of the potential functions can be obtained as follows

$$\left. \begin{aligned} A(k) &= \frac{k(k^2 - \gamma_s^2)\Sigma_1 - i\gamma_s k^2(\Sigma_2 - \Sigma_3)}{\mu[(k^2 - \gamma_s^2)^2 + 4\gamma_p \gamma_s k^2]} \\ B(k) &= -\frac{\Sigma_2 + \Sigma_3}{2\mu\gamma_s} \\ C(k) &= \frac{(k^2 - \gamma_s^2)(\Sigma_2 - \Sigma_3) - 4i\gamma_p k\Sigma_1}{2\mu[(k^2 - \gamma_s^2)^2 + 4\gamma_p \gamma_s k^2]} \end{aligned} \right\} \quad (3)$$

where Σ_1 , Σ_2 and Σ_3 are the respective values in the wave number domain of the Hankel transformation of $\sigma_{zz}^n(r)|_{z=0}$, $\sigma_{rz}^n(r)|_{z=0} - i\sigma_{\theta z}^n(r)|_{z=0}$ and $\sigma_{rz}^n(r)|_{z=0} + i\sigma_{\theta z}^n(r)|_{z=0}$ with orders of n to $n - 2$ (i is the imaginary unit).

The only parameters required in this solution process are the Young's modulus, the Poisson's ratio and the density of the bedrock, which are relatively convenient to obtain.

2.3 Validation of the non-uniform input motion calculation method

The solution obtained using the proposed non-uniform input motion calculation method can be validated against the previously discussed FEM solution in Figs. 4 and 5. The distribution of the peak acceleration in Fig. 4 and the time histories at points A and B in Fig. 5 obtained using the proposed method are all in good agreement with the FEM solution, indicating that the solution is satisfactory under the assumption that the underlying bedrock is linear elastic and homogeneous. The current proposed method is much more computationally efficient compared to the FEM solution. For the FEM solution without any particular treatment of the boundaries, the size of the computation model is proportional to the wave velocity and duration of the motion in order to eliminate the influence of the wave reflected by the truncated boundary. In the verification example, the input acceleration time history that only lasts 0.5 s requires the model to be greater than $2000 \text{ m} \times 2000 \text{ m} \times 1000 \text{ m}$ in order to guarantee that the reflection wave from the boundaries do not reach the base of the dam during the analysis. If an actual seismic motion input were to be used, the model would need to be much larger, which would be very computationally costly, making the proposed method highly attractive.

2.4 3D dynamic FEM analysis method for CFRDs

Once the displacement time history at the base of the CFRD is obtained, it can be used as the input for 3D FEM analysis of the CFRD under non-uniform seismic motion. The OpenSees platform [23] with a “Multi-Support Excitation Pattern” feature that allows non-uniform ground motions (displacement, velocity and acceleration) to be input at designated nodes is used in this study.

An equivalent viscoelastic model proposed by Shen [33], which has accumulated much application experience in the design and analysis of rockfill dams in China over the past three decades, is adopted in this study for the constitutive model of the rockfill in the dynamic analysis. The dynamic shear modulus G and the damping ratio λ in the model are determined as:

$$G = \frac{G_{\max}}{1 + k_1 \gamma_c}, \quad G_{\max} = k_2 P_a \left(\frac{\sigma'_m}{P_a} \right)^n \quad (4)$$

$$\lambda = \lambda_{\max} \frac{k_1 \gamma_c}{1 + k_1 \gamma_c} \quad (5)$$

where P_a is the standard atmospheric pressure, σ'_m is the mean effective stress, k_1 , k_2 , n and λ_{\max} are model parameters and γ_c is the reference engineering shear strain, which can be calculated using the following expression:

$$\gamma_c = 0.65 (\gamma_d)_{\max} / \left(\frac{\sigma'_m}{P_a} \right)^{1-n} \quad (6)$$

where $(\gamma_d)_{\max}$ is the maximum engineering shear strain during the time period of interest. The engineering shear strain is defined as $\gamma_d = 2\bar{\varepsilon}$, where $\bar{\varepsilon} = \frac{\sqrt{2}}{3} [(\varepsilon_1 - \varepsilon_2)^2 + (\varepsilon_2 - \varepsilon_3)^2 + (\varepsilon_3 - \varepsilon_1)^2]^{\frac{1}{2}}$, and ε_1 , ε_2 and ε_3 are the principal strain values. An iterative solution process is adopted for the dynamic analysis, as the $(\gamma_d)_{\max}$ is an unknown variable beforehand.

The permanent deformation caused by earthquake is calculated using an empirical approach in Shen’s model [33]. The duration of the earthquake is equally divided into several time periods, for which the incremental residual volumetric and shear strains in each time period ($\Delta\varepsilon_{V,R}^j$ and $\Delta\gamma_R^j$, where the superscript j is the number of the time period, similarly hereinafter) are calculated using the following expressions:

$$\Delta\varepsilon_{V,R}^j = c_1 (\gamma_c^j)^{c_2} \exp(-c_3 S_l^2) \frac{\Delta N_e^j}{1 + N_e} \quad (7)$$

$$\Delta\gamma_R^j = c_4 (\gamma_c^j)^{c_5} S_l^2 \frac{\Delta N_e^j}{1 + N_e} \quad (8)$$

where S_l is the shear stress level defined as $S_l = \sigma_1 - \sigma_3 / (\sigma_1 - \sigma_3)_f$, σ_1 and σ_3 are the major and

minor principle stress values, respectively, and $(\sigma_1 - \sigma_3)_f = 2c \cos \varphi + 2\sigma_3 \sin \varphi / 1 - \sin \varphi$, in which c and φ are the strength parameters of the soil; ΔN_e^j is the effective number of loading cycles in a period, which is defined as $\Delta N_e^j = \sum_i \Delta\gamma_d^i / (\gamma_d)_{\max}^j$, where i is the number of time steps in the concerned time period; and N_e is the accumulated effective number of effective loading cycles; c_1 , c_2 , c_3 , c_4 and c_5 are model parameters. The residual stress within the dam and concrete face can then be calculated based on the residual displacement.

This method for calculating the dynamic response and permanent deformation of rockfill dams was presented in detail by Shen [33]. Although this nonlinear model is relatively simple and does not take into consideration many aspects of rockfill behavior, including plasticity and anisotropy, it is able to reflect many of the important mechanical characteristics of rockfill and has been widely used as a standard practice in the analysis of rockfill dams in China [4, 5, 9, 11–13, 15, 27, 34, 37, 39, 42, 43, 51].

2.5 Simulation setup

Combining the non-uniform input motion obtained using the method proposed in Sect. 2.2 with the FEM analysis method in Sect. 2.4, the response of CFRDs subjected to non-uniform input motion can be studied. In this study, a simplified CFRD model is used to conduct such investigation. Figure 6 shows the finite element mesh of the dam, which consists of 5936 nodes and 5720 hexahedron elements. The dam model is assumed to be made of uniform rockfill with a concrete face slab lain on the upstream surface (Fig. 6). The concrete face slab is modeled as linear elastic, with Young’s modulus of 30 GPa and Poisson’s ratio of 0.167. The parameters used in the dynamic and residual deformation analysis for the rockfill material of the CFRD are listed in Table 2, which are the parameters of the major rockfill material zone for Gushui CFRD [38].

A total of 23 simulations are conducted in this study, as listed in Table 3. Simulation #1 is a benchmark simulation using uniform seismic input with shaking direction along the river. Figure 7a shows the acceleration time history of the input motion in simulation #1, which has a peak acceleration of 1.65 m/s^2 . In simulation #2, the CFRD model is subjected to non-uniform ground motion input induced by a vertically propagating incident SH wave with an incidence angle of zero vibrating along the direction of the river (y direction). In order to allow for comparisons between simulations #1 and #2, the incident SH wave in simulation #2 guarantees that the acceleration at the surface of the free-field distant from the river valley to be the same as that in simulation #1, following the same comparison standard as that proposed by Zhang et al. [52]. This

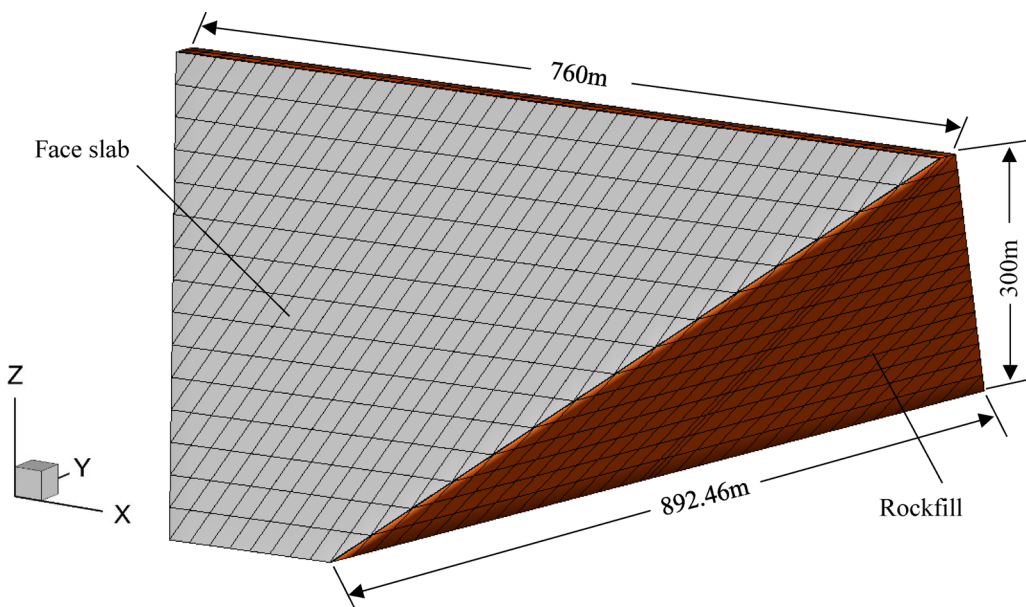


Fig. 6 FEM model of a concrete face rockfill dam

Table 2 Dynamic calculation parameters

Material	k_2	λ_{\max}	μ_d	k_1	n	c_1	c_2	c_3	c_4	c_5
Rockfill	2660	0.21	0.2	39	0.444	0.0084	0.81	0	0.1082	0.62

Table 3 The simulation program

Project ID	Input mode	Incident wave category	Angle of incidence
#1	Uniform	—	—
#2	Non-uniform	SH	0°
#3	Non-uniform	SH	15°
#4	Non-uniform	SH	30°
#5	Non-uniform	SH	45°
#6	Non-uniform	SH	60°
#7	Non-uniform	SH	75°
#8	Non-uniform	SH	85°
#9	Non-uniform	SH	90°
#10	Non-uniform	P	0°
#11	Non-uniform	P	15°
#12	Non-uniform	P	30°
#13	Non-uniform	P	45°
#14	Non-uniform	P	60°
#15	Non-uniform	P	75°
#16	Non-uniform	P	85°
#17	Non-uniform	P	90°
#18	Non-uniform	SV	0°
#19	Non-uniform	SV	15°
#20	Non-uniform	SV	30°
#21	Non-uniform	SV	35.26°

Table 3 (continued)

Project ID	Input mode	Incident wave category	Angle of incidence
#22	Non-uniform	SV	45°
#23	Non-uniform	SV	60°
#24	Non-uniform	SV	75°
#25	Non-uniform	SV	85°
#26	Non-uniform	SV	90°

The angle of incidence is the angle between incident direction and vertical direction

standard ensures the consistency of the vibration process at the free-field surface points distant from the valley. Figure 7b plots the acceleration time history at the free-field surface distant from the valley calculated using the proposed method for simulation #2, which is almost exactly the same as that of simulation #1.

Simulations #2–#9, simulations #10–#17 and simulations #18–#26 are designed to investigate the response of CFRDs under incident SH, P and SV waves from different directions, respectively (Table 3). In order to keep the horizontal vibration component along the river for all three types of incident waves, the incident plane for P and SV waves ($y-z$ plane) is different from that for SH waves ($x-$

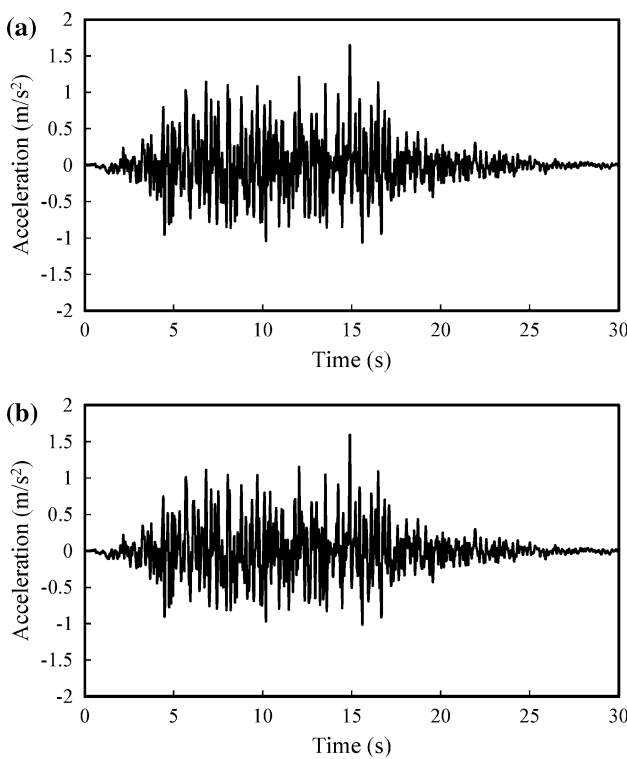


Fig. 7 Input acceleration time history: **a** acceleration for uniform input, **b** acceleration at the free-field surface distant from the valley calculated for simulation #2

z plane). Figure 8a shows the direction of the incidence of SH waves. Figure 8b shows the direction of the incidence of P or SV waves.

3 CFRD response under non-uniform input motion

Typical results from simulation #2 can be compared with those of simulation #1 to analyze the seismic response of CFRDs under non-uniform input motion, under the notion that the acceleration at the surface of the free-field distant from the river valley should be the same for both non-uniform and uniform input motion simulations.

Figure 9 shows the peak value of the acceleration of the points on the base of the dam for non-uniform and uniform input motion, which reflects the intensity of the input motion. The non-uniform input motion at the base of the dam is generally smaller than that of the uniform input. Figure 10 shows the acceleration time histories of several points on the boundary, which reflect the non-uniformity of the input motion. Figure 11a, b shows the contours of the peak acceleration on the vertical plane along the dam axis for simulations #1 and #2, respectively. It can be observed that the peak acceleration under non-uniform ground motion input is overall smaller. Figure 12 plots the

acceleration time histories at the center of the dam crest in both simulations #1 and #2. Again, the acceleration under non-uniform input is smaller. These results suggest that both the acceleration input at the base of the dam and the acceleration within the dam are smaller for simulation #2 with a non-uniform ground motion.

Figure 13a, b shows the contours of the peak dynamic compressive stress perpendicular to the dam slope within the concrete face slab under uniform and non-uniform input, respectively. In similar fashion, Fig. 14a, b shows the contours of the corresponding peak dynamic tensile stress. Under non-uniform input, both the compressive and the tensile stress perpendicular to the dam slope within the concrete face slab are in general smaller, which is to be expected considering the difference in the acceleration of the CFRD. However, Fig. 14c shows the difference of the peak dynamic tensile stress of the face slab between simulations #1 and #2, it can be seen that around the edges of the concrete face slab, especially in the corners, the tensile stress of the concrete face slab under non-uniform input is greater. This increase in tensile stress under non-uniform input could be caused by the phase and amplitude difference between the input motions at different positions. The difference in tensile stress due to non-uniform input motion should be considered in design as a potential threat to the safety of the seepage control system, as such locations are weak links of the seepage control system where failures are exceptionally detrimental and difficult to repair.

Figure 15a, b shows the residual settlement contours on the cross section in the middle of the dam for simulations #1 and #2, respectively. Similar to the acceleration results, the residual settlement under non-uniform input is smaller than that under a comparable uniform input.

Table 4 shows the maximum peak acceleration, peak dynamic compressive and tensile stress of the concrete face and post-earthquake compressive and tensile stress of the concrete face. The post-earthquake tensile stress of the face along the upstream slope exhibits as much as 45% relative difference between non-uniform and uniform, while all other results showed around 10–40% relative differences. These results indicate that current design and analysis approaches of using uniform input could result in seismic responses that deviate significantly from reality, and the design for high CFRDs based on non-uniform input is necessary. It can be seen that under the conditions of study in this paper, the dynamic response and residual deformation induced by uniform input is in general larger than those induced by non-uniform input, suggesting current design and analysis methods to be conservative. However, the tensile stress results shown in Fig. 14c also suggest that the seismic response obtained under uniform input is not globally conservative, where the dynamic tensile stress around the edges of the concrete face slab could be larger

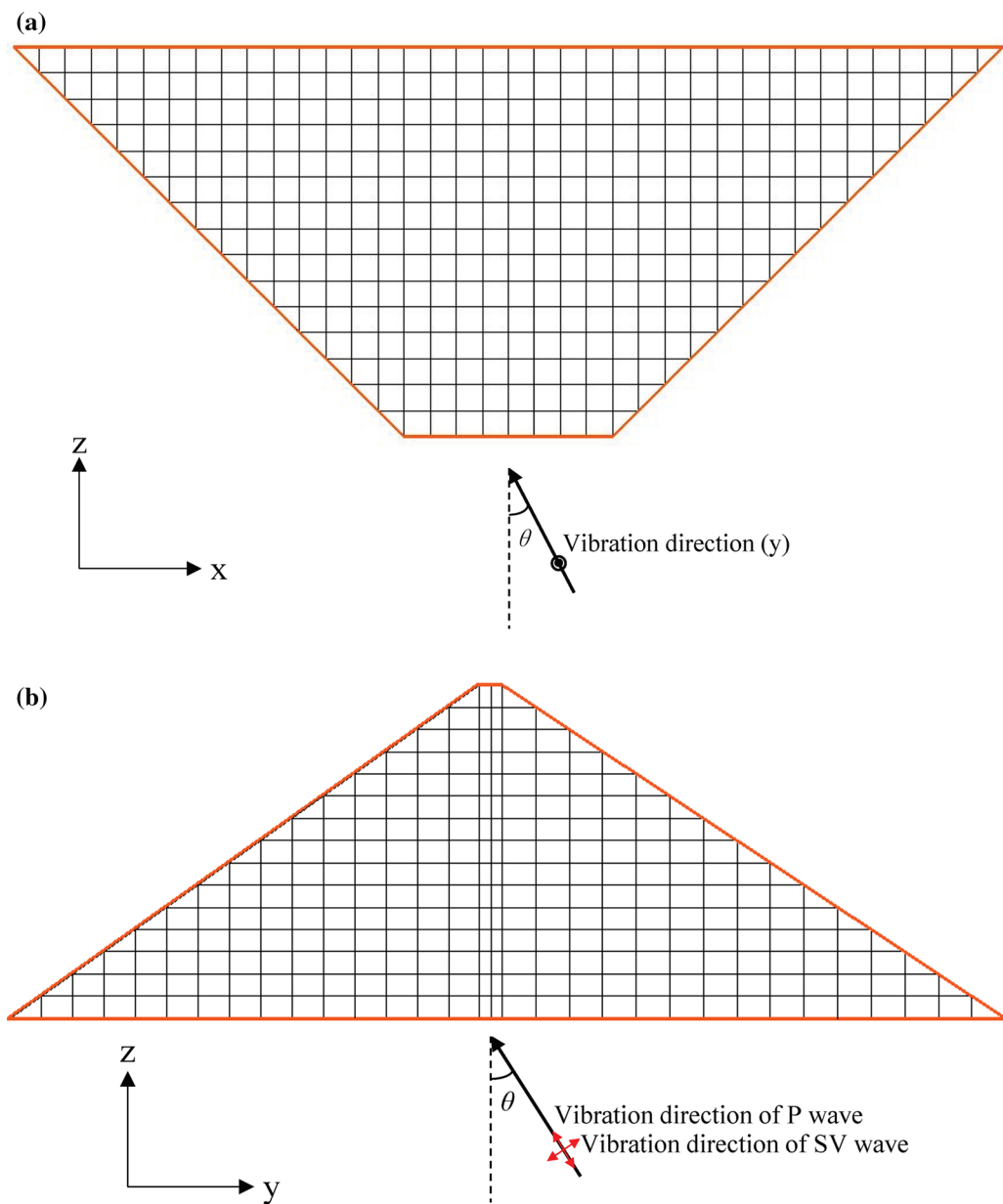


Fig. 8 Direction of incident waves: **a** SH wave, **b** P or SV wave

under non-uniform input compared with that under uniform input. The greater dynamic tensile stress at the edges could provide explanations for some of the damage observed by Zhang et al. near the abutment of the Zipingpu CFRD after the Wenchuan earthquake [48].

4 Effects of the angle of incidence on the response of the dam

The distinct difference between the response of CFRDs under non-uniform and traditional uniform input motions indicate that it is worthwhile to investigate the influence of

the major characteristics of the non-uniform input motion. Hence, the response of CFRDs under three different waveforms (SH, SV and P waves) and different incident angles are analyzed and compared through simulations #2–#26.

Figures 16 and 17 show the relationship of the peak dynamic response, including the maximum average acceleration (the maximum value of the average acceleration within the CFRD during the earthquake, used to reflect the overall response of the dam) and the peak dynamic stress of the face along slope of the face, and the maximum residual settlement with the incident angle θ under SH wave input. It can be observed that for SH wave, θ has little influence

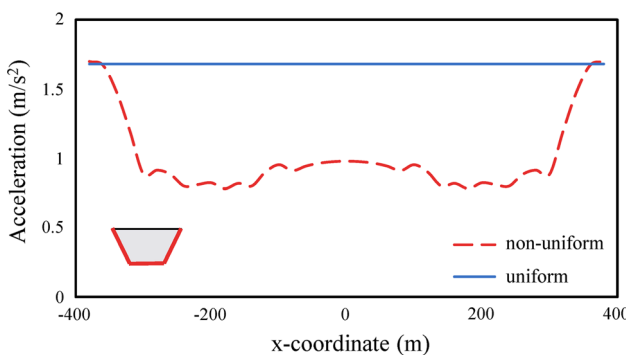


Fig. 9 Peak value of the acceleration at the points along the intersection of the base and axis plane of the dam for non-uniform and uniform input motion

on both the peak dynamic response and the residual settlement of the dam.

Similarly, Figs. 18 and 19 show the dependency of the peak dynamic response and the maximum residual settlement on the incident angle θ under P wave input. It can be observed that for a P wave input, as θ increases from 0° to

90° , the responses exhibit little variation initially, but decrease significantly when θ is close to 90° and become zero when θ equals to 90° because the calculated input motion becomes zero.

Figures 20 and 21 show the relationship of the peak dynamic response and the maximum residual settlement with the incident angle θ under SV wave input. Under SV wave input, the responses all peaked when θ reaches a critical value of 35.26° , and decrease significantly as θ increases beyond the critical value and become zero again for SV wave input when θ equals to 90° because the calculated input motion becomes zero.

The simulation results in Figs. 16, 17, 18, 19, 20 and 21 suggest that the incident angle has different effects on the response of CFRDs depending on the input waveform. These effects of the incident angle for different waveforms can be explained analytically by analyzing the influence of the incident angle on the intensity of the input motion. To analytically analyze the relationship between the incident angle and the response of the dam for different input

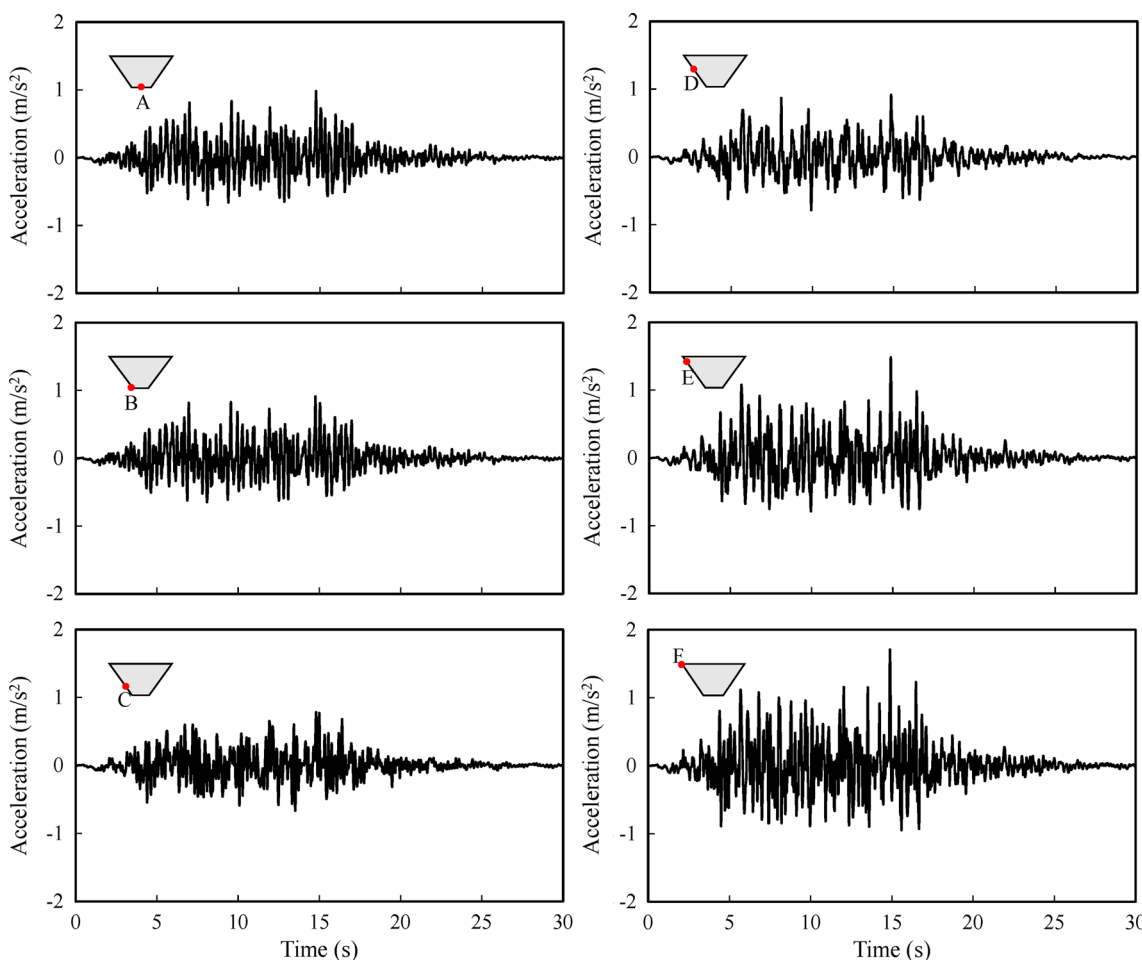


Fig. 10 Acceleration time histories of several points on the boundary. The x-coordinates of the points A, B, C, D, E and F are 0, -80 , -180 , -280 , -340 and -380 m, respectively

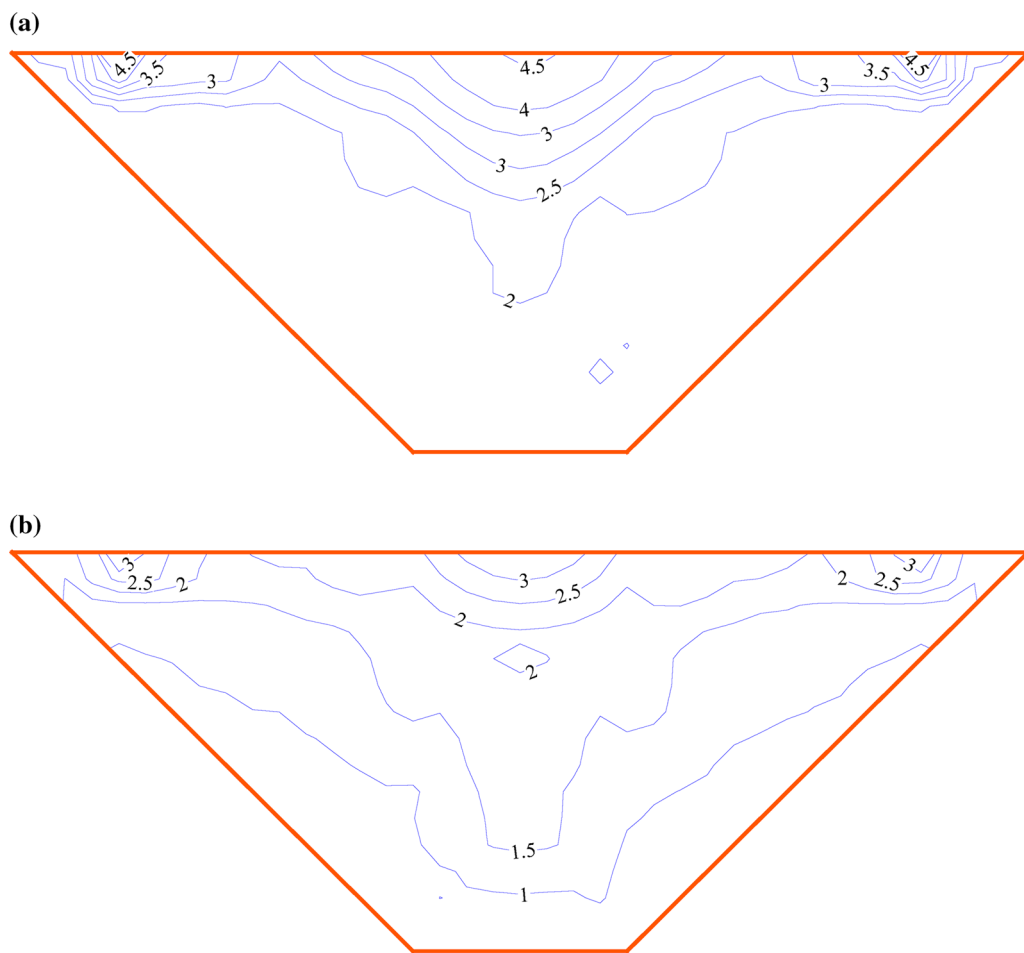


Fig. 11 The peak y direction acceleration (m/s^2) contours for: **a** Uniform input (simulation #1), **b** Non-uniform input (simulation #2)

waveforms, we investigate the amplification factor, which is defined as the ratio between the free-surface displacement amplitude and that of the original incident wave. This amplification factor can be deduced for different waveforms as functions of the incident angle and can reflect the intensity of the overall input motion at the base of the dam, which in turn affects the response intensity of the dam. The greater the amplification factor is, the greater the dam response is.

(1) Incident SH waves

When the incident angle of the SH wave in $x-z$ plane is θ_0 , the potential functions of the incident and the reflected wave are (the subscript 1 represents incidence and the subscript 2 represents reflection, the same below)

$$\left. \begin{aligned} \varphi_1 &= A_0 \exp(ik(x \sin \theta_0 - z \cos \theta_0)) \\ \varphi_2 &= A_0 \exp(ik(x \sin \theta_0 + z \cos \theta_0)) \end{aligned} \right\} \quad (9)$$

where k stands for the wave number, and A_0 is the coefficient of the potential functions. The free field is described as

$$\left. \begin{aligned} u_x^f &= 0 \\ u_y^f &= 2A_0 \cos(kz \cos(\theta_0)) \exp(ikx \sin \theta_0) \\ u_z^f &= 0 \end{aligned} \right\} \quad (10)$$

For z equal to zero, we can obtain the amplitude of the surface point

$$A_{\text{surf}} = 2A_0 \quad (11)$$

The amplitude of the incident wave is

$$A_{\text{inc}} = A_0 \quad (12)$$

Then we can obtain the amplification factor

$$\alpha = \frac{A_{\text{surf}}}{A_{\text{inc}}} = 2 \quad (13)$$

It can be seen that the amplification factor is a constant independent of the incident angle, which is consistent with the simulation results shown in Figs. 16, 17 in general.

(2) Incident P waves

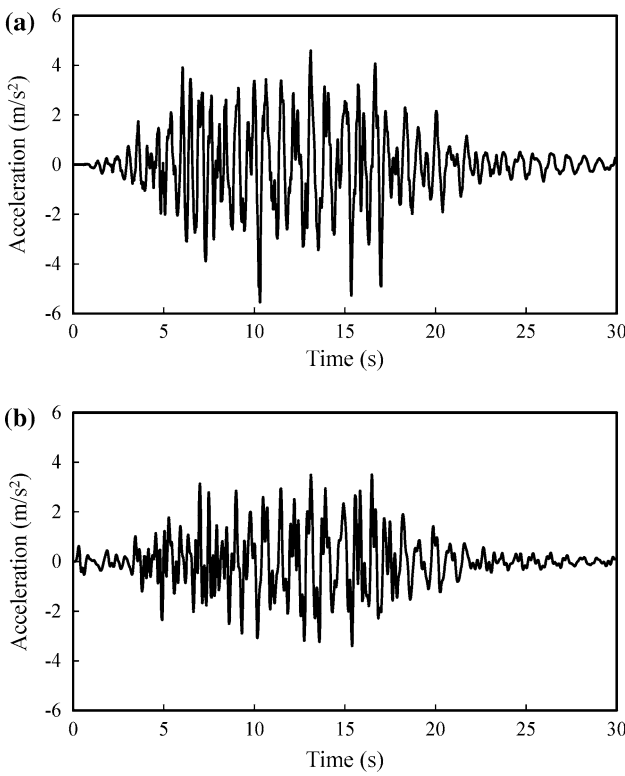


Fig. 12 The peak y direction acceleration (m/s^2) time histories at the center of the dam crest for: **a** uniform input (simulation #1), **b** non-uniform input (simulation #2)

When the incident angle of the P wave in x - z plane is θ_0 , the potential functions of the incident and the reflected wave are

$$\left. \begin{aligned} \varphi_1 &= A_1 \exp(ik(x - p_1 z)) \\ \varphi_2 &= A_2 \exp(ik(x + p_1 z)) \\ \psi_2 &= B_2 \exp(ik(x + p_2 z)) \end{aligned} \right\} \quad (14)$$

where k stands for the x -direction wave number; A_1 , A_2 and B_2 are the potential function coefficients of the incident P wave, the reflected P wave and reflected SV wave, respectively; $p_1 = (c^2/c_p^2 - 1)^{\frac{1}{2}}$, $p_2 = (c^2/c_s^2 - 1)^{\frac{1}{2}}$, $c = c_p/\sin \theta_0$ and

$$\left. \begin{aligned} A_2 &= \frac{4p_1p_2 - (1 - p_2^2)^2}{4p_1p_2 + (1 - p_2^2)^2} \\ B_2 &= \frac{-4p_1(1 - p_2^2)}{4p_1p_2 + (1 - p_2^2)^2} \end{aligned} \right\} \quad (15)$$

The free field is described as

$$\left. \begin{aligned} u_x^f &= ik(\varphi_1 + \varphi_2 - p_2(-\psi_2)) \\ u_y^f &= 0 \\ u_z^f &= -ik(p_1(\varphi_1 - \varphi_2) + \psi_2) \end{aligned} \right\} \quad (16)$$

For z equal to zero, we can obtain the amplitude of the surface point

$$A_{\text{surf}} = k \sqrt{(A_1 + A_2 + p_2 B_2)^2 + (p_1 A_1 - p_1 A_2 + B_2)^2} \quad (17)$$

The amplitude of the incident wave is

$$A_{\text{inc}} = k A_1 \sqrt{(1 + p_1^2)} \quad (18)$$

Then we can obtain the amplification factor

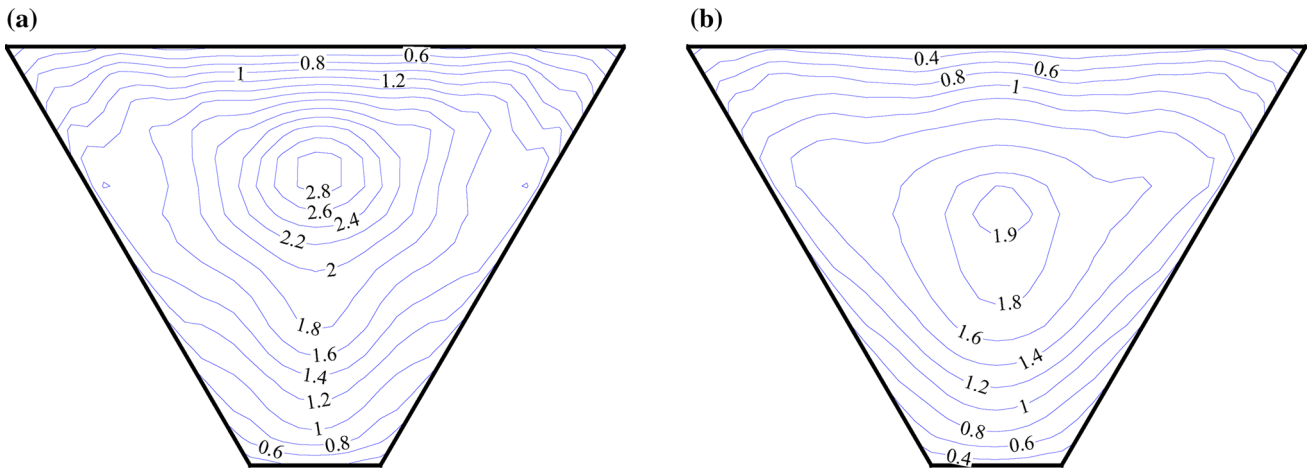


Fig. 13 Peak dynamic compressive stress (MPa) perpendicular to the dam slope in: **a** uniform input (simulation #1), **b** non-uniform input (simulation #2)

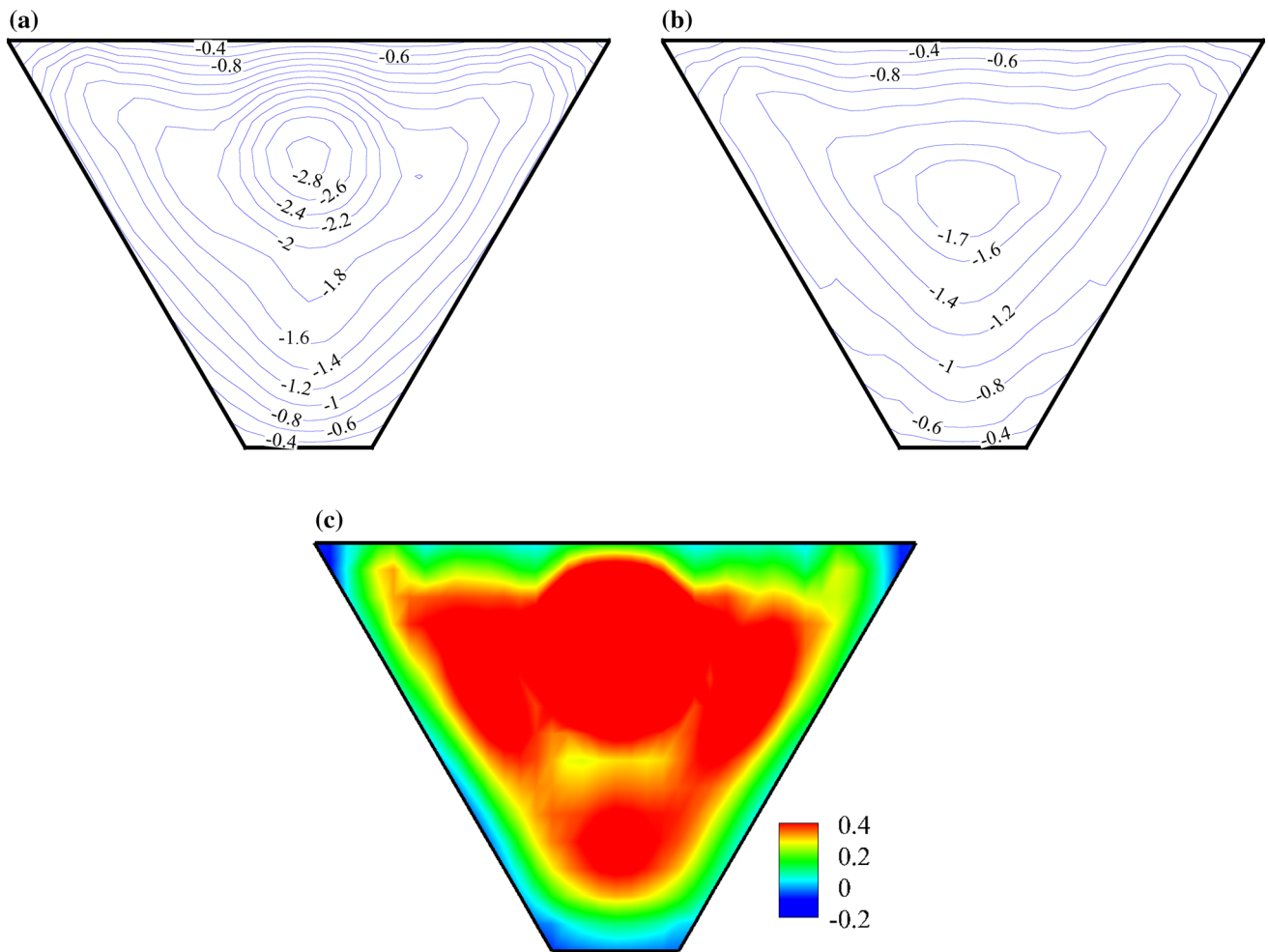


Fig. 14 Peak dynamic tensile stress perpendicular to the dam slope: **a** uniform input (simulation #1), **b** non-uniform input (simulation #2) and **c** difference between non-uniform and uniform input

$$\alpha = \frac{A_{\text{surf}}}{A_{\text{inc}}} = \frac{\sqrt{(A_1 + A_2 + p_2 B_2)^2 + (p_1 A_1 - p_1 A_2 + B_2)^2}}{A_1 \sqrt{(1 + p_1^2)}} \quad (19)$$

Since all the variables in the expression of α is only related to the incidence angle and the Poisson's ratio of the medium, we can rewrite Eq. (19) as

$$\alpha = f_P(\theta, v) \quad (20)$$

The relationships between the amplification factor α and the incident angle θ for the incidence of P waves with different Poisson's ratio are shown in Fig. 22a–c. α decreases significantly after the incident angle increases beyond a certain angle, which depends on the Poisson's ratio. Comparing the results shown in Figs. 18, 19 with the relationship for P waves shown in Fig. 22b where the Poisson's ratio is the same with that in the dynamic FEM analysis, a consistent pattern of significant decrease near 90° incident angle can be observed.

(3) Incident SV waves

When the incident angle of the SV wave in $x-z$ plane is θ_0 , the potential functions of the incident and the reflected wave are

$$\left. \begin{array}{l} \varphi_2 = A_2 \exp(ik(x + p_2 z)) \\ \psi_1 = B_1 \exp(ik(x - p_2 z)) \\ \psi_2 = B_2 \exp(ik(x + p_2 z)) \end{array} \right\} \quad (21)$$

where k stands for the x -direction wave number; A_2 , B_1 and B_2 are the potential function coefficient of the reflected P wave, the incident SV wave and reflected SV wave, respectively; $p_1 = (c^2/c_p^2 - 1)^{\frac{1}{2}}$, $p_2 = (c^2/c_s^2 - 1)^{\frac{1}{2}}$, $c = c_s/\sin \theta_0$ and

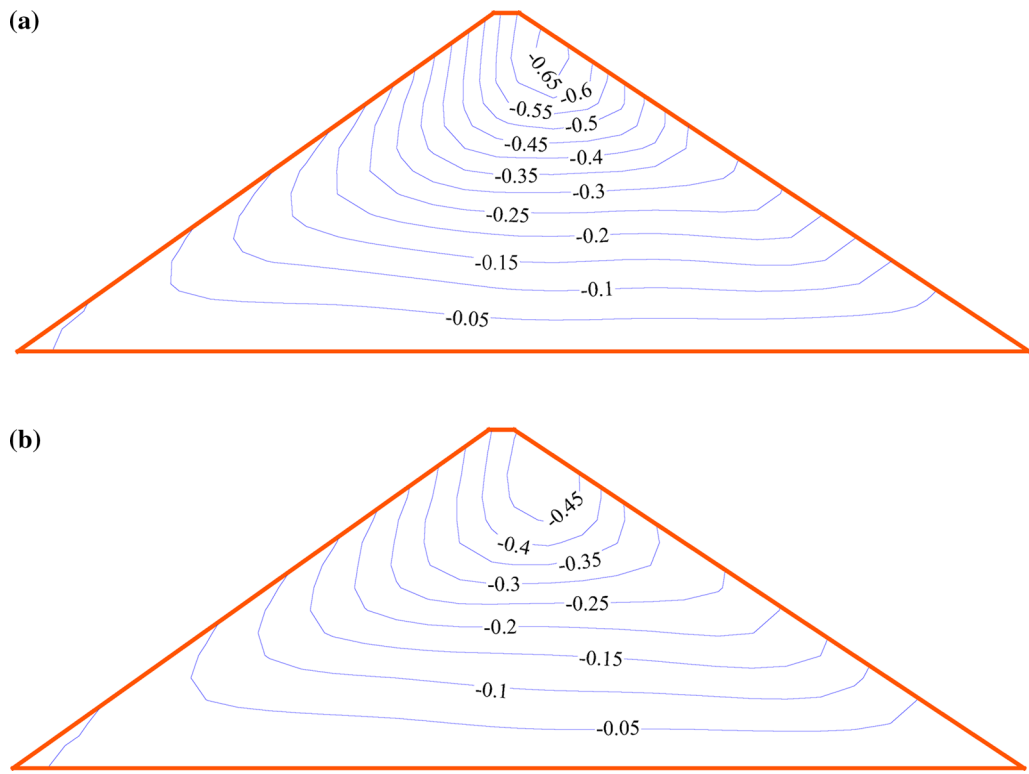


Fig. 15 Residual settlement (m) in: **a** uniform input (simulation #1), **b** non-uniform input (simulation #2)

Table 4 The peak response of the model CFRD under uniform input and non-uniform input in simulations #1 and #2

Items	Uniform input (simulation #1)	Non-uniform input (simulation #2)	Percentage of the difference (%)
a_y (m/s^2)	7.15	5.57	28
s (m)	0.68	0.5	26
σ_{dxt} (MPa)	- 1.25	- 1	20
σ_{dyp} (MPa)	1.12	0.73	35
σ_{dst} (MPa)	- 2.88	- 1.79	38
σ_{dsp} (MPa)	2.88	1.94	33
σ_{pxt} (MPa)	- 3.83	- 3.14	18
σ_{pxp} (MPa)	10.95	8.85	19
σ_{pst} (MPa)	- 0.49	- 0.27	45
σ_{psp} (MPa)	8.33	7.33	12

a_y acceleration along the river, s residual settlement, σ_{dxt} dynamic tensile stress of the face along the axis of the dam, σ_{dyp} dynamic pressure stress of the face along the axis of the dam, σ_{dst} dynamic tensile stress of the face along the slope of the face, σ_{dsp} dynamic pressure stress of the face along the slope of the face, σ_{pxt} post-earthquake tensile stress of the face along the axis of the dam, σ_{pxp} post-earthquake pressure stress of the face along the axis of the dam, σ_{pst} post-earthquake tensile stress of the face along the slope of the face, σ_{psp} post-earthquake pressure stress of the face along the slope of the face

$$\left. \begin{aligned} \frac{A_2}{B_1} &= \frac{4p_2(1-p_2^2)}{4p_1p_2 + (1-p_2^2)^2} \\ \frac{B_2}{B_1} &= \frac{4p_1p_2 - (1-p_2^2)^2}{4p_1p_2 + (1-p_2^2)^2} \end{aligned} \right\} \quad (22)$$

The free field is described as

$$\left. \begin{aligned} u_x^f &= ik(\varphi_2 - p_2(\psi_1 - \psi_2)) \\ u_y^f &= 0 \\ u_z^f &= -ik(p_1(-\varphi_2) + \psi_1 + \psi_2) \end{aligned} \right\} \quad (23)$$

For z equal to zero, we can obtain the amplitude of the surface point

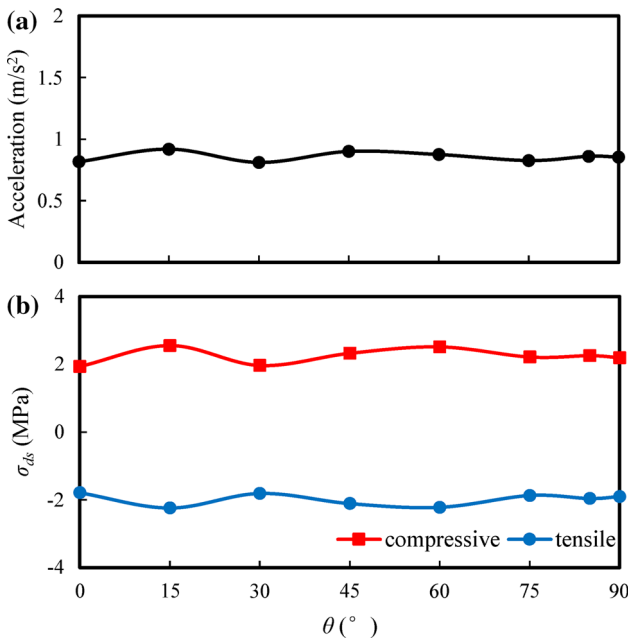


Fig. 16 The relationship between the peak dynamic response induced by SH waves and the incidence angle θ . **a** is for the maximum average acceleration, and **b** is for the peak dynamic stress of the face along slope of the face

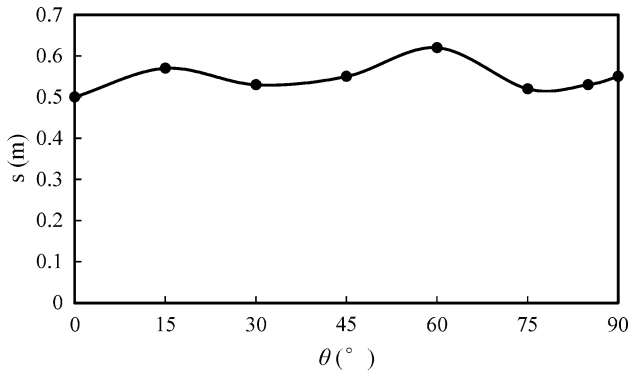


Fig. 17 The relationship between the maximum residual settlement induced by SH waves and the incidence angle θ

$$A_{\text{surf}} = k \sqrt{(A_2 - p_2 B_1 + p_2 B_2)^2 + (p_1 A_2 - B_1 - B_2)^2} \quad (24)$$

The amplitude of the incident wave is

$$A_{\text{inc}} = kB_1 \sqrt{(1 + p_2^2)} \quad (25)$$

Then we can obtain the amplification factor

$$\alpha = \frac{A_{\text{surf}}}{A_{\text{inc}}} = \frac{\sqrt{(A_2 - p_2 B_1 + p_2 B_2)^2 + (p_1 A_2 - B_1 - B_2)^2}}{B_1 \sqrt{(1 + p_2^2)}} \quad (26)$$

Again, we can rewrite Eq. (26) as

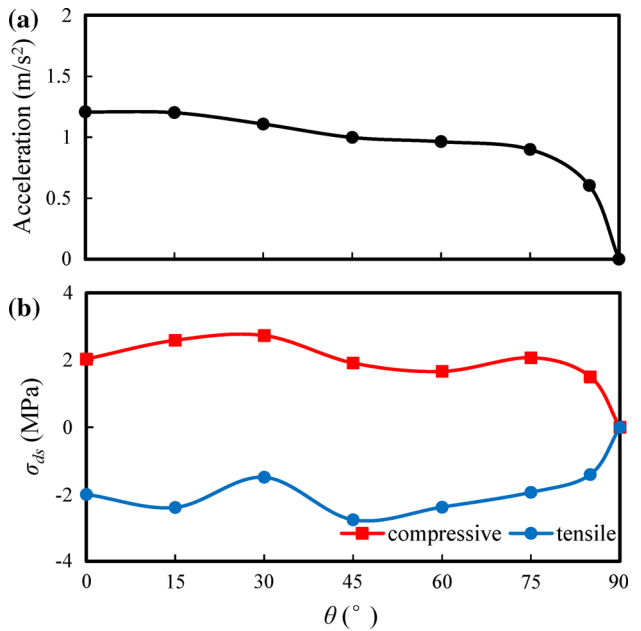


Fig. 18 The relationship between the peak dynamic response induced by P waves and the incidence angle θ . **a** is for the maximum average acceleration, and **b** is for the peak dynamic stress of the face along slope of the face

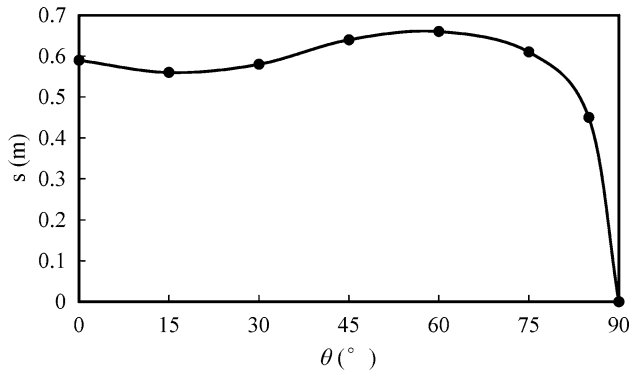


Fig. 19 The relationship between the maximum residual settlement induced by P waves and the incidence angle θ

$$\alpha = f_{SV}(\theta, v) \quad (27)$$

The relationships between the amplification factor α and the incident angle θ for the incidence of SV waves with different Poisson's ratio are also shown in Fig. 22a–c. It can be seen that a peak value occurs at a critical incident angle of $\theta_{cr} = \arcsin(c_s/c_p)$. When the incident angle θ exceeds θ_{cr} , which means $c < c_p$, thus $p_1 = (c^2/c_p^2 - 1)^{\frac{1}{2}}$ is no longer a real number, and the reflected wave is no longer a plane wave. When θ reaches θ_{cr} , the α reaches its peak, and decreases as θ moves away from θ_{cr} to either side. Comparing the results shown in Figs. 20, 21 with the relationship for SV waves shown in Fig. 22b, a consistent pattern can also be observed.

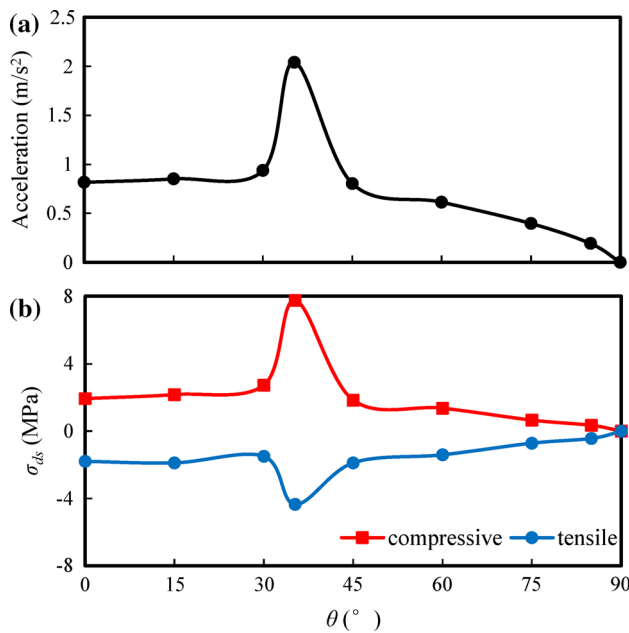


Fig. 20 The relationship between the peak dynamic response induced by SV waves and the incidence angle θ . **a** is for the maximum average acceleration, and **b** is for the peak dynamic stress of the face along slope of the face

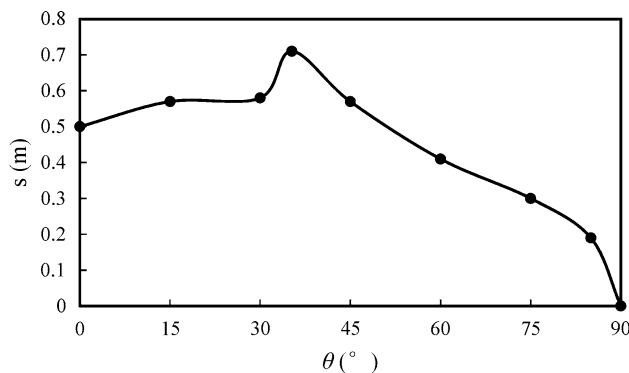
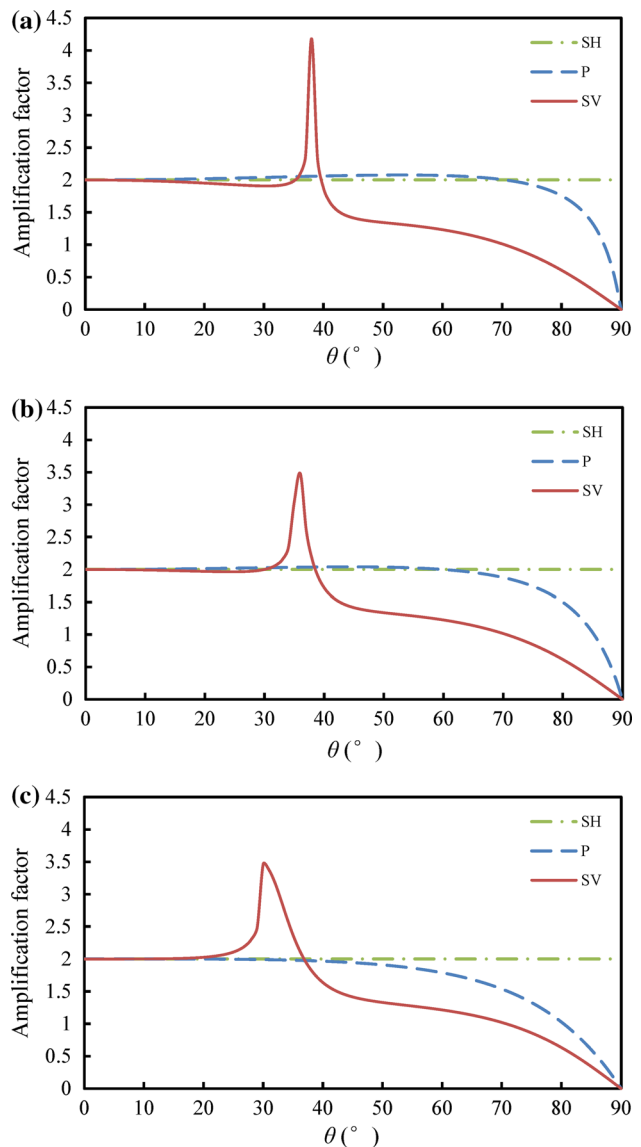


Fig. 21 The relationship between the maximum residual settlement induced by SV waves and the incidence angle θ

The analytical analysis of the influence of incident angle on the amplification factor for different waveforms provides an explanation for dynamic response patterns observed in the FEM simulations, showing the dependency of the intensity of the input motion on the incident angle and waveform (Fig. 22), which is in turn reflected on the seismic response of the CFRD (Figs. 16, 17, 18, 19, 20, 21). It should be pointed out that the analytical analysis shows that the amplification factor α is independent of the frequency of the incident wave, indicating that the conclusions drawn from the analytical analysis and the patterns observed in the FEM simulation are generally applicable to the full frequency spectrum.



5 Conclusions

Analysis of the seismic response of high CFRDs under non-uniform ground motion input is conducted using a novel non-uniform input motion calculation method and nonlinear FEM. The new method adopted in this study has advantages of high calculation efficiency, high precision and numerical stability. The response of CFRDs under uniform and non-uniform input is compared to show the necessity of seismic analysis based on non-uniform input. The influence of the incident angle of seismic waves of different forms is investigated using the proposed simulation method, with an analytical explanation provided for the results.

Simulations conducted using the proposed method shows that when the acceleration at the surface of the free field for dynamic simulations with uniform and non-uniform input is kept consistent, the response of CFRDs under non-uniform input is in general significantly smaller, suggesting current design and analysis methods to be conservative. However, the dynamic tensile stress around the edges of the concrete face slab could be larger under non-uniform input compared with that under uniform input, and pose non-negligible threat to the seepage control system.

The influence of the incident angle on the dynamic response of CFRDs is shown to be dependent on the waveform, while independent of frequency. The dynamic response of CFRDs for SH waves is almost independent of the incident angle, while for P waves the response decreases after the incident angle exceeds an angle that is related to the Poisson's ratio. For SV waves, the response reaches the peak value when the angle reaches the critical angle of $\theta_{cr} = \arcsin(c_s/c_p)$.

The dynamic constitutive model for the rockfill area is a simple nonlinear model. In future studies, high fidelity plasticity constitutive models should be adopted. Wave scattering problem solutions that are able to take into consideration non-uniform bedrock should also be developed. The contact behaviors between rockfill body and concrete face are not considered in this study for simplicity, which may influence the resulting response in the concrete face, possibly increasing both tensile and compressive stresses. It should also be noted that the non-uniform input motion calculation method is developed under the assumption that the bedrock is a homogeneous isotropic linear elastic medium, and the modulus is much larger than that of the rockfill dam.

Acknowledgements The authors gratefully acknowledge the financial support by the National Key Research Program of China (Grant No. 2016YFC1402800), and the National Natural Science Foundation of China (Nos. 51708332 and No. 51678346).

References

- Banerjee P, Mamoon S (1990) A fundamental solution due to a periodic point force in the interior of an elastic half-space. *Earthq Eng Struct Dyn* 19(1):91–105
- Beck JL (1979) Determining models of structures from earthquake records. California Institute of Technology, California
- Chen H, Du X, Hou S (1998) Application of transmitting boundaries to non-linear dynamic analysis of an arch dam-foundation-reservoir system. Dynamic soil-structure interaction: current research in China and Switzerland, pp 115–124
- Chen S, Li G, Fu Z (2013) Safety criteria and limit resistance capacity of high earth-rock dams subjected to earthquakes. *Chin J Geotech Eng* 35(1):59–65 (in Chinese)
- Chen S, Wang T, Fu Z, Wei K (2015) Seismic damage mechanism of high concrete face rockfill dams. *Chin J Geotech Eng* 37(11):1937–1944 (in Chinese)
- Dakoulas P (1993) Response of earth dams in semicylindrical canyons to oblique SH waves. *J Eng Mech* 119(1):74–90
- Dakoulas P, Hashmi H (1992) Wave passage effects on the response of earth dams. *Soils Found* 32(2):97–110
- De Alba PA, Seed HB, Retamal E et al (1988) Analyses of dam failures in 1985 Chilean earthquake. *J Geotech Eng* 114(12):1414–1434
- Diao Z, Ma W, Liu L, Wang J (2013) 3-D finite element analysis on seismic response of Jinbo mountain concrete faced rockfill dam. *J Chongqing Jiaotong University Nat Sci* 32(2):285–289 (in Chinese)
- Dibaj M, Penzien J (1969) Response of earth dams to traveling seismic waves. *J Soil Mech Found Div* 95(2):541–560
- Ding X, Kong G, Li P et al (2012) Finite element analysis of dynamic response of Maoergai earth-rockfill dam in earthquake disaster. *Disaster Adv* 5(4):1004–1009
- Ding X, Kong G, Liu H et al (2013) Numerical analysis on seismic response of Shiziping earth-rockfill dam. *Disaster Adv* 6:94–101
- Ding X, Liu H, Yu T et al (2013) Nonlinear finite element analysis of effect of seismic waves on dynamic response of Shiziping dam. *J Cent South Univ* 20:2323–2332
- Eurocode 8: Design of structures for earthquake resistance-Part 2: Bridges. 1998
- Fei K, Liu H (2010) Secondary development of ABAQUS and its application to static and dynamic analyses of earth-rockfill dam. *Rock Soil Mech* 31(3):881–890 (in Chinese)
- Haeri S, Karimi M (2004) Three-dimensional dynamic analysis of concrete faced rockfill dam with spatial variable ground motion. *J Dam Eng* 14(4):257–294
- Hall WS (1994) Boundary element method//the boundary element method. Springer, Netherlands, pp 61–83
- Haroun M, Abdel-Hafiz E (1987) Seismic response analysis of earth dams under differential ground motion. *Bull Seismol Soc Am* 77(5):1514–1529
- ICOLD Bulletin 120 (2001) Design features of dams to effectively resist seismic ground motion, Committee on Seismic Aspects of Dam Design. ICOLD, Paris
- Lamb H (1904) On the propagation of tremors over the surface of an elastic solid. *Philosophical Transactions of the Royal Society of London. Series A, containing papers of a mathematical or physical character*, vol 203, pp 1–42
- Li B, Cheng L, Deeks A et al (2005) A modified scaled boundary finite-element method for problems with parallel side-faces. Part I. Theoretical developments. *Appl Ocean Res* 27(4):216–223
- Liao W, Teng T, Yeh C (2004) A series solution and numerical technique for wave diffraction by a three-dimensional canyon. *Wave Motion* 39(2):129–142
- McKenna F, Fenves GL (2001) OpenSees manual, PEER Center <http://OpenSees.berkeley.edu>
- National Research Institute for Earth Science and Disaster Prevention website. Retrieved 1 Jan 2015, from http://www.kyoshin.bosai.go.jp/kyoshin/quake/index_en.html
- Pao YH, Mow CC (1973) Diffraction of elastic waves and dynamic stress Concentrations. Crane, Russak, New York
- Papalou A, Bielak J (2001) Seismic elastic response of earth dams with canyon interaction. *J Geotech Geoenviron Eng* 127(5):446–453
- Qi L, Chen Q, Cai J (2015) Effect of seismic permanent deformation on safety and stability of earth-rock dam slope. *Trans Tianjin Univ* 21:167–171

28. Sanchez-Sesma FJ (1983) Diffraction of elastic waves by three-dimensional surface irregularities. *Bull Seismol Soc Am* 73(6):1621–1636
29. Sanchez-Sesma FJ, Miguel AB, Ismael H (1985) Surface motion of topographical irregularities for incident P, SV, and Rayleigh waves. *Bull Seismol Soc Am* 75(1):263–269
30. Seed HB, Lee KL, Idriss IM et al (1975) The slides in the San Fernando dams during the earthquake of February 9, 1971. *Journal of Geotechnical and Geoenvironmental Engineering*, 101(ASCE# 11449 Proceeding)
31. Seiphoori A, Haeri S, Karimi M (2011) Three-dimensional nonlinear seismic analysis of concrete faced rockfill dams subjected to scattered P, SV, and SH waves considering the dam–foundation interaction effects. *Soil Dyn Earthq Eng* 31(5):792–804
32. Shen Z, Xu Z (1983) Seismic response analysis of geotechnical structures considering the traveling wave. *J Hydraul Eng* 11:37–43 (in Chinese)
33. Shen Z, Xu G (1996) Deformation behavior of rock materials under cyclic loading. *J Nanjing Hydraul Res Inst* 2:143–150 (in Chinese)
34. Shi ZM, Wang YQ, Peng M et al (2015) Characteristics of the landslide dams induced by the 2008 Wenchuan earthquake and dynamic behavior analysis using large-scale shaking table tests. *Eng Geol* 194:25–37
35. Tian J (2003) Earth dam's response to multi-point input seismic incitation and relative researching method. Hohai University, Nanjing (in Chinese)
36. Verdugo R, Sitar N, Frost JD et al (2012) Seismic performance of earth structures during the February 2010 Maule, Chile, earthquake: dams, levees, tailings dams, and retaining walls. *Earthq Spectra* 28(S1):S75–S96
37. Wang X, Kang F, Li J et al (2012) Inverse parametric analysis of seismic permanent deformation for earth-rockfill dams using artificial neural networks. *Math Probl Eng* 2012:383749
38. Wang F, Yang Z, Zhou J et al (2014) Brief introduction of the safety and key technology research for 300 m high concrete face rockfill dam. In: Proceedings of the high concrete face rockfill dam safety research and progress on soft rock dam technology, Nanjing, pp 19–22 (in Chinese)
39. Wang X, Kang F, Li J (2014) Back analysis of earthquake-induced permanent deformation parameters of earth-rock dams. *Rock Soil Mech* 35(1):279–286 (in Chinese)
40. Wong H (1982) Effect of surface topography on the diffraction of P, SV and rayleigh waves. *Bull Seismol Soc Am* 72(4):1167–1183
41. Wu Z (2007) Study of the worst seismic motion input for earth-dam seismic stability under the oblique incidence condition. PhD dissertation, China Earthquake Administration, Harbin (in Chinese)
42. Yang G, Liu K, Liu Y (2013) Research on the maximum anti-seismic capability of high earth rock-fill dam under strong earthquake. *Disaster Adv* 6:9–15
43. Yang J, Li G, Shen T (2014) Dynamic response analysis of high CFRD under complex terrain conditions. *Rock Soil Mech* 35(11):3331–3337 (in Chinese)
44. Yao Y, Liu T, Zhang J (2016) A new series solution method for two-dimensional elastic scattering by a canyon in half-space. *Soil Dyn Earthq Eng* 89:128–135
45. Zemanian AH (1968) Generalized integral transformations. Interscience Publishers, New York
46. Zerva A, Ang AHS, Wen YK (1986) Development of differential response spectra for lifeline seismic analysis. *Probab Eng Mech* 1(4):208–218
47. Zhang S (2014) Research on the effect of incident directions of seismic waves on the dynamic response of rock-fill dam. Dalian University of Technology, Dalian (in Chinese)
48. Zhang J (2015) Geotechnical aspects and seismic damage of the 156-m-high Zipingpu concrete-faced rockfill dam following the Ms 8.0 Wenchuan earthquake. *Soil Dyn Earthq Eng* 76:145–156
49. Zhang L, Chopra AK (1991) Three-dimensional analysis of spatially varying ground motions around a uniform canyon in a homogeneous half-space. *Earthq Eng Struct Dyn* 20(10):911–926
50. Zhang L, Chopra AK (1991) Impedance functions for three-dimensional foundations supported on an infinitely-long canyon of uniform cross-section in a homogeneous half-space. *Earthq Eng Struct Dyn* 20(11):1011–1027
51. Zhang G, Zhang J (2009) Numerical modeling of soil–structure interface of a concrete-faced rockfill dam. *Comput Geotech* 36(5):762–772
52. Zhang C, Pan J, Wang J (2009) Influence of seismic input mechanisms and radiation damping on arch dam response. *Soil Dyn Earthq Eng* 29(9):1282–1293
53. Zhou W, Hua J, Chang X et al (2011) Settlement analysis of the Shuibuya concrete-face rockfill dam. *Comput Geotech* 38(2):269–280